Exploring solar wind origins and connecting plasma flows from Parker Solar Probe to 1 AU:
non-spherical source surface and Alfvénic fluctuations

Olga Panasenco,[1] Marco Velli,[2] Raffaella D'Amicis,[3] Chen Shi,[2] Victor Réville,[2, 4] Stuart D. Bale,[5, 6, 7, 8]
Samuel T. Badman,[5, 6] Justin Kasper,[9] Kelly Korreck,[10] J. W. Bonnell,[6] Thierry Dudok de Wit,[11]
Keith Goetz,[12] Peter R. Harvey,[6] Robert J. MacDowall,[13] David M. Malaspina,[14] Marc Pulupa,[6]
Anthony W. Case,[10] Davin Larson,[6] Roberto Livi,[6] Michael Stevens,[15] and Phyllis Whittlesey[6]

[1]Advanced Heliophysics, Pasadena, CA, USA
[2]UCLA Earth Planetary and Space Sciences Department, Los Angeles, CA, USA
[3]National Institute for Astrophysics (INAF), Institute for Space Astrophysics and Planetology (IAPS),
Via del Fosso del Cavaliere 100, I-00133 Rome, Italy; Serco S.p.A, Via Sciadonna 24, I-00044 Frascati, Italy
[4]IRAP, Université Toulouse III - Paul Sabatier, CNRS, CNES, Toulouse, France
[5]Physics Department, University of California, Berkeley, CA 94720-7300, USA
[6]Space Sciences Laboratory, University of California, Berkeley, CA 94720-7450, USA
[7]The Blackett Laboratory, Imperial College London, London, SW7 2AZ, UK
[8]School of Physics and Astronomy, Queen Mary University of London, London E1 4NS, UK
[9]University of Michigan, Ann Arbor, MI, USA
[10]Smithsonian Astrophysical Observatory, Cambridge, MA, USA
[11]LPC2E, CNRS and University of Orléans, Orléans, France
[12]School of Physics and Astronomy, University of Minnesota, Minneapolis, MN 55455, USA
[13]Solar System Exploration Division, NASA/Goddard Space Flight Center, Greenbelt, MD, 20771
[14]Laboratory for Atmospheric and Space Physics, University of Colorado, Boulder, CO 80303, USA
[15]Smithsonian Astrophysical Observatory, Cambridge, MA 02138 USA

ABSTRACT

The magnetic field measurements of the FIELDS instrument on Parker Solar Probe (PSP) have shown intensities, throughout its first solar encounter, that require a very low source surface height ($R_{SS} \leqslant 1.8\ R_\odot$) to be reconciled with magnetic field measurements at the Sun via potential field extrapolation (PFSS). However, during PSP's second encounter the situation went back to a more classic source surface height ($R_{SS} \leqslant 2.5\ R_\odot$). Here we use high-resolution observations of the photospheric magnetic field (SDO/HMI) to calculate neutral lines and boundaries of the open field regions for source surface heights from 1.2 to 2.5 $R_\odot$, using an evolving PFSS model and the measured solar wind speed to trace the source of the wind observed by PSP to the low corona and photosphere. We adjust R_{SS} to get the best match for the field polarity over the period October - November 2018 and March - April 2019, finding that the best fit for the observed magnetic field polarity inversions requires a non-spherical source surface. The geometry of the coronal hole boundaries for different R_{SS} is tested using the PSP perihelion passes, 3D PFSS models and LASCO/C2 observations. We investigate the sources of stronger than average magnetic fields, and times of Alfvénic fast and slow wind. Only some of the strongly Alfvénic slow wind streams seen by PSP survive and are observed at 1 AU: the origins and peculiar topology of the background in which they propagate is discussed.

Corresponding author: Olga Panasenco
panasenco.olga@gmail.com

1. INTRODUCTION

Parker Solar Probe (Fox et al., 2016) completed its first perihelion pass on November 6th 2018, reaching a distance of $35.7\,R_\odot$ from the Sun, closer by almost a factor two than previous man-made exploration. Observations of the magnetic field and velocity show that PSP crossed the heliospheric current sheet multiple times (see Figure 1), and that the speed of the wind was predominantly very slow. Remarkably, the wind displayed a strongly dominant outward propagating spectrum of Alfvénic fluctuations throughout the encounter, a feature that is rarely seen in very slow solar wind streams at Earth and beyond.

Here we use the simplest possible magnetic field extrapolation, namely a Potential Field Source Surface (PFSS) model, to locate the solar footpoints of the solar wind seen by Parker Solar Probe (PSP) throughout its first perihelion passage, and then explore possible connections with the solar wind seen at L1 and at Earth, and discuss the different, evolved properties, of the solar wind seen at such greater distances in conjunction with the source regions on the Sun. **PFSS extrapolations have proven to provide a qualitatively correct model of the overall topology of the magnetic field at the source surface (SS), but may place the neutral line and pseudostreamers at slightly different latitudes to where they should be according to coronagraph data (see, e.g. Morgan & Habbal, 2010 and Morgan, 2011). We therefore supplement the information provided by PFSS with coronograph images and other plasma properties, such as the presence of Alfvén waves propagating away from the Sun and the corresponding magnetic field-velocity field correlation, to back up the correct determination of the neutral line crossings.**

The first perihelion passages of Parker Solar Probe occurred during the minimum phase of the present solar cycle. During this phase, a spacecraft located in the ecliptic at 1 AU would generally detect alternating streams of faster and slower wind. Beyond the speed differences, these two solar wind regimes show many other specific characteristics, from the large scale structure (Schwenn 1990) to composition (Geiss et al. 1995), to the spectral properties of the embedded turbulent fluctuations (see reviews by Tu & Marsch 1995; Bruno & Carbone 2013) and last but not least, different origins on the Sun. In this regard, although it is well known

that most of the fast solar wind streams originate from polar coronal holes, the origin(s) of the slow wind are still a (e.g. Wang & Sheeley 1990; Antonucci et al. 2005; Abbo et al. 2016) mysterious, and indeed the classification of the solar wind outflow uniquely in terms of wind speed is probably too simplistic (e.g. Von Steiger 2008; Zhao et al. 2009; Ko et al. 2018; Stansby et al. 2019; D'Amicis et al. 2019).

One important feature characterizing solar wind fluctuations, especially within the main portion of fast solar wind streams, is the presence of large amplitude fluctuations showing an Alfvénic nature. The adjective Alfvénic refers to the presence in the wind of large amplitude velocity and magnetic field fluctuations with the correlation between them corresponding to Alfvén waves propagating away from the Sun. In addition, relative density fluctuations are suppressed together with fluctuations in magnetic field magnitude, so that the magnetic field vector apex locally moves on the surface of a sphere (Matteini et al. 2015).

Based on this definition, fast wind is usually found to be more Alfvénic than slow wind (Belcher & Davis 1971; Belcher & Solodyna 1975). However, recent results (D'Amicis & Bruno 2015; D'Amicis et al. 2019) have shown that the slow solar wind can also sometimes show a high degree of Alfvénicity, with velocity and magnetic field fluctuations as large as those found in the fast wind. It is important to note that this kind of slow wind was studied using measurements at 1 AU where one would expect a degradation of the Alfvénic correlation due to the solar wind expansion. In addition, the identification of this Alfvénic slow wind was found on a statistical basis over the maximum of solar cycle 23. D'Amicis et al. (2019) suggested the idea that a possible solar source for this Alfvénic slow solar wind would lie in low-latitude small coronal holes (in agreement with Wang 1994; Neugebauer et al. 1996; Wang & Ko 2019; Wang & Panasenco 2019) that were a ubiquitous feature of the solar surface during maximum of solar cycle 23 (Platten et al. 2014).

An Alfvénic slow wind stream was observed in a portion of wind preceding a fast stream during the perihelion passage of the Helios mission at solar activity minimum (Marsch et al. 1981). A detailed characterization of this kind of wind was developed recently by Stansby et al. (2019b) and Perrone et al. (2019). In contrast to the findings of D'Amicis et al. (2019), the amplitude of the fluctuations was smaller in this case
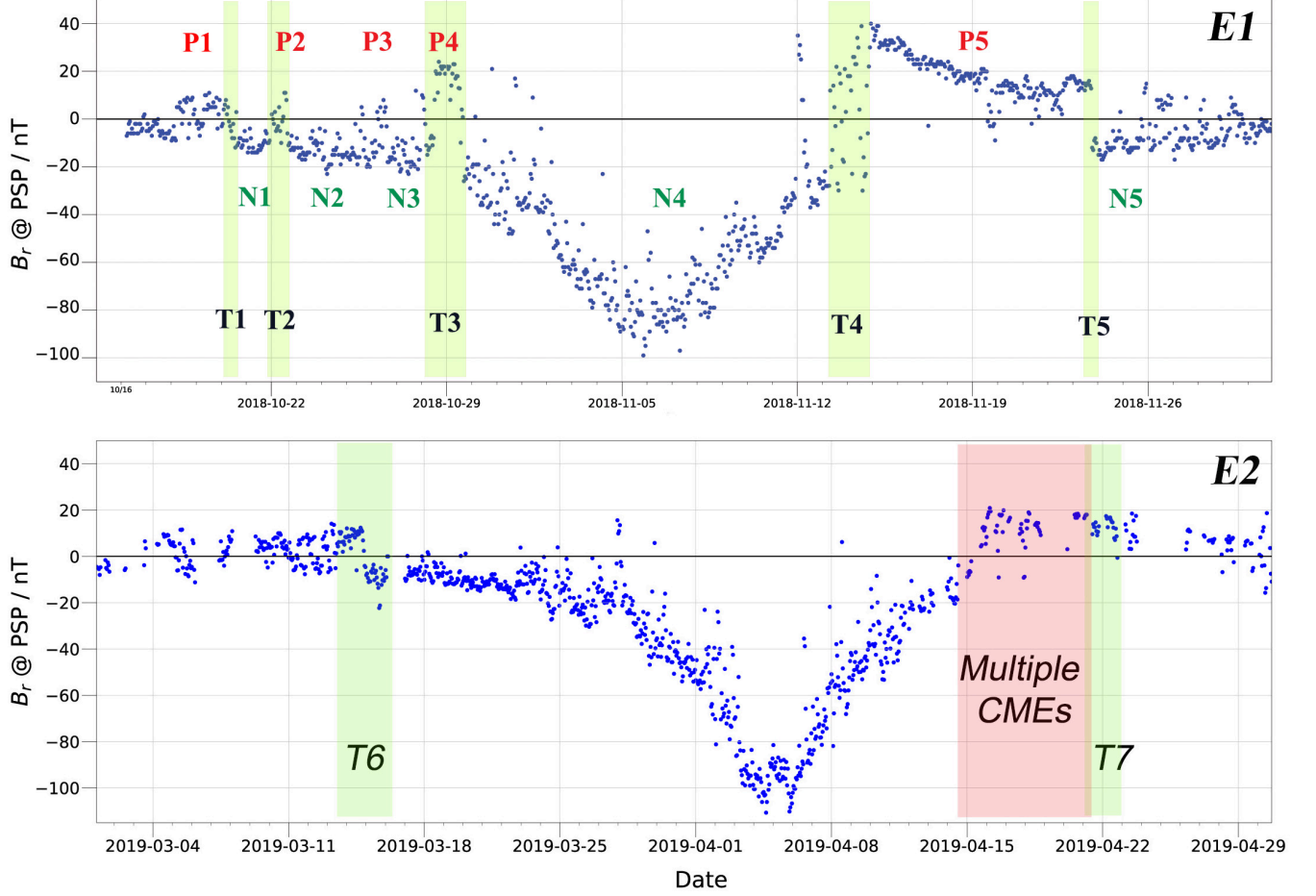
Figure 1. The B_r measurements for Encounters 1 and 2 (labeled E1 and E2). Five positive (P1-P5) and five negative (N1-N5) periods were identified for E1. One negative and two positive periods for E2. The transition periods of changing polarity labeled T1-T7 and defined in Table 1. Multiple CMEs occurred during E2, the time period shaded in red.

than that seen in typical fast wind but still larger than that of the typical slow wind. The solar wind seen by PSP over the first perihelion encounter appears to be an example of slow Alfvénic solar wind. In this case, the Alfvénic slow wind observed by PSP originated from a very rapidly expanding small equatorial coronal hole adjacent to a pseudostreamer configuration, i.e. a multipolar closed configuration opening into a unipolar field (Wang et al. 2007; Panasenco & Velli 2013; Panasenco et al. 2019). The corresponding solar wind at Earth showed this property only partially, providing evidence for the evolution and destruction of Alfvénicity in a slow solar wind stream as it traveled from the Sun to 1 AU.

In the next section the magnetic field measurements from the first PSP encounter and the connectivity from the solar coronal footpoints of PSP into the solar wind is discussed and the source surface height required to properly match the polarity transitions observed by the space-

craft and map them back to the Sun is determined. Although this height is lower than the "standard" accepted values, we show that it is actually depends on the region above the Sun, along the lines of Levine et al. (1982). For the purpose of clarity we have labeled the polarities (P for positive, N for negative) and the transitions (T) we will discuss explicitly in Figure 1 (and further identified in Table 1). The choice of these transitions, seen in the Figure as labeled green shadings over the 1-hour median field values plotted throughout the time intervals of the first (*E1*) and second (*E2*) encounters, was made to identify clear, reliable crossings of the heliospheric polarity inversion sheet, avoiding time-dependent disturbances such as blobs or CMEs. For *E1*, we do not discuss the P3/N3 transition as there are multiple crossing within the hour median time, and similarly for *E2* we

limit the discussion to the two transitions **T6** and **T7**. *E2* is discussed mainly to contrast the resulting source-surface with the more surprising case of *E1*.

Table 1.   Transition Periods for E1 and E2, PSP B_r

Transition	Time period (2018-2019)	Polarity
T1	Oct 20	P1/N1
T2	Oct 22	N1/P2/N2
T3	Oct 28-29	N3/P4/N4
T4	Nov 13-14	N4/P5
T5	Nov 23	P5/N5
T6	Mar 15	P/N
T7	Apr 22	N/P

2. PFSS RECONSTRUCTIONS OF THE SOLAR MAGNETIC FIELD, NON-SPHERICAL SOURCE SURFACE, AND PSP SOLAR WIND SOURCES

In our study we use the PFSS model developed by Schrijver & De Rosa (2003). As a lower boundary condition, this PFSS model incorporates magnetic field maps produced by an evolving surface-flux transport model based on magnetic fields observed by the Helioseismic and Magnetic Imager (HMI) (e.g. Scherrer et al., 2012; Schou et al., 2012) on the Solar Dynamics Observatory (SDO) and evolves these fields in accordance to empirical prescriptions for the differential rotation, meridional flows, and convective dispersal processes. In addition to the SS height, PFSS depends crucially on the effective resolution of the fields on the solar disk and the treatment of the polar fields, that are difficult to observe and often not used directly in the PFSS extrapolation model (in this case, the magnetogram assimilation window is limited to the area within ± 60 degrees of disk center, and polar fields rely on large-scale transport processes). For the PFSS discussed here, the effective magnetogram resolution used for extrapolation is 8 arcseconds ($\simeq 5800$ km on the Sun, significantly less than a typical supergranule diameter). In addition, the PFSS was updated with polar flux transport modeling corrections to better fit the observed magnetic fields and neutral lines (Liu et al., 2012) of the next to last deep minimum in 2012. With a fixed resolution and the defined flux transport model, PFSS now depends only on the source surface height. Again, the real coronal fields involve importantly dynamic layers, from the chromosphere through the transition region to the corona itself, where volume currents play a role and the PFSS model can not be expected to reproduce the real solar coronal magnetic field precisely. It is for this reason that identifying the solar origin of solar wind parcels must rely on other factors as well, discussed further below.

Coronal heating and solar wind acceleration lead to the stretching and opening of magnetic field lines into the solar wind. The simplest models for the magnetic expansion consist in the potential field source-surface model and its variants: a height is specified at which all magnetic field lines become open and radial, the source surface height, typically located at a height $R_{SS} = 2.5$ $R_\odot$ from the center of the Sun, and the field from the photosphere to the corona is reconstructed, on the basis of the radial field at the surface, as a potential field. The radius of the source-surface is a free parameter of the model. By construction, because the magnetic field in the shell between the photosphere and source-surface is potential, the magnetic field in that region falls as $1/R^3$ or faster, depending on the multipolar expansion, i.e. on the strength and distribution of magnetic polarities. On the other hand, beyond the source surface, the field becomes radial, and decays as $1/R^2$. As a consequence, adjusting the source-surface height changes both the total amount of open flux as well as the magnitude of the magnetic field at a given radius, and this can be done to fit the average values observed by different spacecraft. In addition, the location and shape of the Heliospheric Current Sheet (HCS) will change. For example, Todd Hoeksema at Wilcox Solar Observatory has been producing HCS maps for two SS: 2.5 and 3.25 $R_\odot$. Averaging over solar cycles, the best source surface radius has been found to be at about 2.5 $R_\odot$, although $R_{SS} = 3.25$ $R_\odot$ gave a slightly better result when comparing to the high latitude Ulysses measurements during the 1994 polar pass in the middle of the declining phase. In this period, the Sun presents fewer sunspots but the global field may be stronger and more organized topologically. During the cycles 22 and 23 minimum periods the source surface radius values of 1.8 $R_\odot$ and 1.9 $R_\odot$ produced the best results (Lee et al. 2011). Badman et al. (2020 this issue) carries out an extensive investigation with PFSS reconstructions using different solar magnetic field sources (GONG, HMI). One of the main conclusions is that in order to accurately capture the relative magnitude of the radial magnetic field measured by PSP, and sufficiently open mid-latitude and equatorial coronal holes, the source surface must be placed at $R_{SS} \leqslant 2.0 \, R_\odot$. Levine et al. (1977), using data for the entire *Skylab* period in 1973,
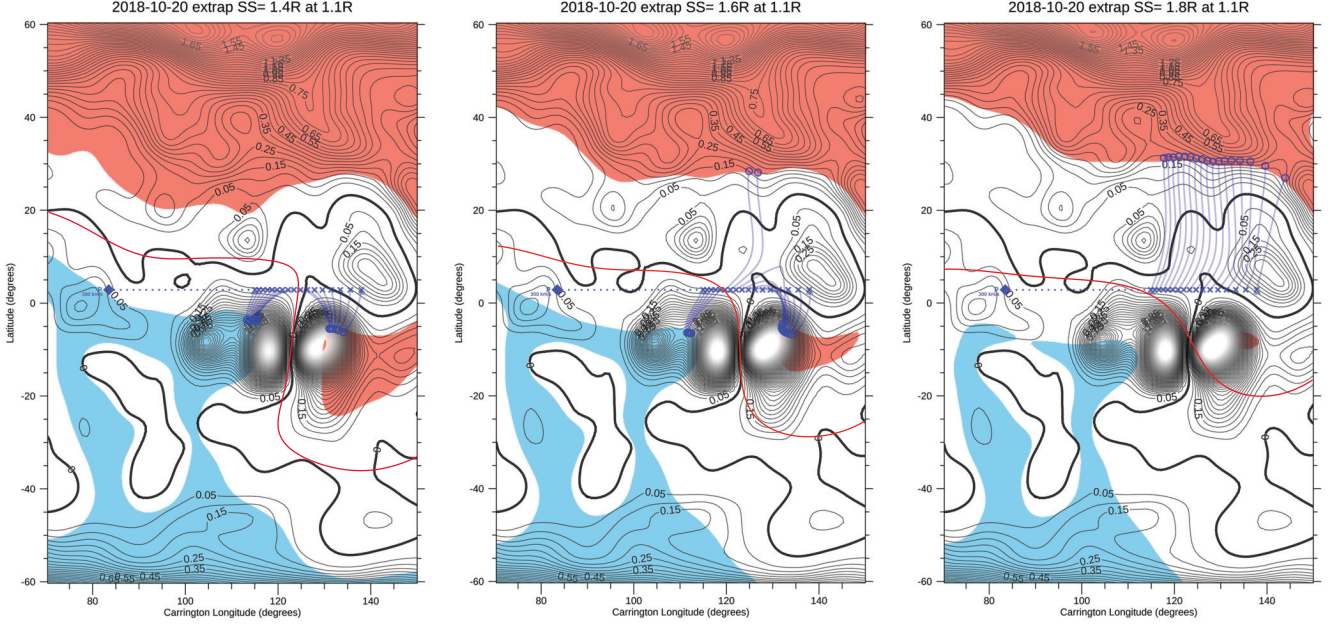
Figure 2. PFSS B^2 contour maps and magnetic field line foot-points for PSP for polarity transition period T1. The projection of the PSP location (blue diamond) is projected onto the source surface (blue crosses) and down to the solar wind source region (blue circles) calculated for the height R = 1.1.R$_\odot$ and solar wind speeds of 300 ± 80 km s^{-1} (in increasing/decreasing steps of 10km/s). From the left to right panel R$_{SS}$ = 1.4, 1.6, 1.8 $R_\odot$. Open magnetic field regions are shown in blue (negative) and red (positive), the neutral line at R = 1.1.R$_\odot$ is in bold black **while the SS neutral line is shown thin red**.

found that extrapolation of an average magnetic field strength in the equatorial plane at 1 AU which is near the observed average value requires a source surface near 1.5 R$_\odot$ during the cycle 20 minimum. The present cycle 24 solar minimum is also very weak, and indeed as we shall see the optimal source surface height will also be quite low.

The PSP/FIELDS (Bale et al. 2016; Bale et al. 2019) observations of the radial magnetic field are summarized in Figure 1, showing the intensity and sign of the field expressed in terms of the modal field value from bins comprising 1 hour of data (i.e. each data point is the modal value of $B_r \pm 30$ min), so that all the rapidly varying transient structures are removed. In the figures, the label N is used to identify periods of negative polarity, P for different periods of positive polarity and T for the transition periods (not all, but those of interest, as specified in Table 1). One can see that from October 18 through November 26 the polarity of the field changed at least 7 times, while throughout the whole of the perihelion pass, from October 30 through November 15, Probe found itself in a region of negative polarity.

In the overall weak field of the current solar minimum during the first encounter we can identify two specific areas on the Sun with a magnetic field stronger than average: the new active regions NOAA AR 12724 and AR 12725 at Carrington Longitude $\sim 125°$; and a de-

caying and heavily dispersed AR 12713 (first emerged five rotations earlier) at Carrington Longitude $\sim 320°$.

In the following the footpoints of the wind seen by PSP will be traced down to their source regions on the Sun, and compared with the magnetic field polarity at a height of 1.1 R$_\odot$ as obtained by PFSS extrapolation with different SS heights. **In order to trace PSP observations to the sources back at the Sun, we carry out a ballistic extrapolation with the wind speed measured at PSP, corrected up to $\pm$ 80 km s^{-1}, in bins of 10 km s^{-1}, down to the SS height, at which point we follow the individual PFSS field lines down towards the Sun for all ballistic speeds. The result, for the transition period T1, is illustrated in Figure 2. The plots show magnetic pressure iso-contours at 1.1 R$_\odot$, with shaded color indicating coronal holes with the respective polarity (blue, negative and red, positive). Overplotted is the direct radial projection of PSP, as a blue diamond, while the the ballistic extrapolations down to the source surface are shown by the blue crosses on the plot.** The crosses are then traced down to 1.1 R$_\odot$ using the PFSS field lines, and the results are plotted as open circles. One first thing to remark is how irregular, the neutral line (in bold) is, with large latitudinal excursions, the height of the SS notwithstanding (for the three pan-
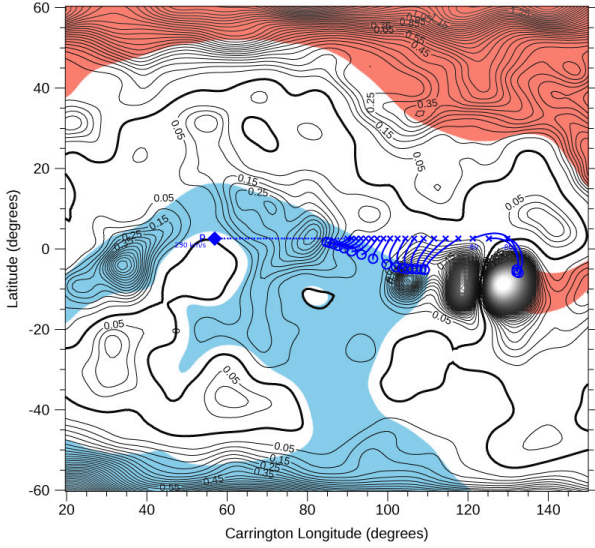
Figure 3. PFSS B^2 contour maps and solar wind foot-points along the PSP trajectory for polarity transition period T2. The projection of PSP location (blue diamond) on the source surface (blue crosses) and down to the solar wind source region (blue circles) calculated for the height R = 1.1.$R_\odot$ and solar wind speed 230 ± 80 km s^{-1}. The projection calculated for the $R_{SS} = 1.6$ $R_\odot$. Open magnetic field regions shown in blue (negative) and red (positive), the neutral line is in bold.

els, from left to right, R_{SS} goes from $1.4 - 1.8$ $R_\odot$. As the SS moves upward coronal holes shrink in size, as seen from the decreasing areas shaded in blue and red moving from the left to the right panel. By inspecting the different panels, one can see that the SS height of 1.8 $R_\odot$ (right panel) can not correctly identify the transition from one polarity to the other as seen in interval T1, rather PSP then remains connected to the positive polarity of the low boundary of the polar coronal hole at higher latitudes. On the other hand, lower source surface heights show that small changes in solar wind speed lead to a quick transition from one polarity to the other (left and center panel). The best fit for T1 is $R_{SS} = 1.6$ $R_\odot$. Figures 3 - 7 provide analogous plots for the polarity transitions labeled T2 - T7.

Figure 3 illustrates the T2 transition from negative to positive and back N1/P2/N2. A R_{SS} height of 1.6 $R_\odot$ was used to reproduce negative-positive-negative jump, as the PSP trajectory moves leftwards on the plot. For the period T2, PSP magnetic footpoints were located mostly in the negative open field regions N1 and N2. To reproduce the observed short jump back to the positive polarity P2 the solar wind speed of 230 ± 80 km s^{-1} was used, reproducing the short-lived magnetic connection back to the positive polarity region, that is the observed

P2 result. The positive region P2 is the same as P1 in Figure 2.

Figure 4 illustrates transition T3 (N3/P4/N4), when the PSP magnetic footpoints moved across very weak magnetic field regions with $B_r = 0.4$ - 1.3 G at 1.1 $R_\odot$, which is at least an order of magnitude smaller **compared to the near equatorial magnetic field observed during solar maximum in cycle 24 in 2014 (Figure 5 in Janardhan et al. 2018)**. To reproduce the polarity transition observed by the PSP/FIELDS instrument the R_{SS} height is reduced to 1.2 $R_\odot$. The left panel in Figure 4 illustrates the transition T3 (from negative to positive polarity): the PSP magnetic footpoints connected to the small equatorial coronal hole with negative polarity (blue shade) and to the open field area of the polar coronal extension of positive polarity (red shade). The right panel shows the transition P4/N4: the negative polarity region N4 is the west boundary of the big equatorial coronal hole above which PSP will spend the following two weeks October 30 - November 15, 2018. For the N3 negative polarity region the SS was lowered to $R_{SS} = 1.2$ $R_\odot$ and field lines projected from the source surface down to $B_r = 1.05$ $R_\odot$. The transition N3/P4 is especially sensitive to the source surface height and easily disappears for higher R_{SS}. However the transition P4/N4 is captured for R_{SS} up to1.6 $R_\odot$. **This conclusion is also supported by Badman et al. (2020 this issue).**

Figure 5 illustrates the protracted transition period T4 (N4/P5), during which PSP is leaving the co-rotation region above the negative open field area to which the spacecraft was connected for the two previous weeks. Figure 1 shows that the duration of the transition period T4 is 2 days and twice as long as all simple polarity transitions. To investigate the longer period transition the PSP magnetic footpoint projections were modeled for two consecutive days Nov 14 - 15, 2018 and for three different R_{SS} heights of 1.6, 1.8 and 2.0 $R_\odot$. The goal was to find the R_{SS} height required to connect PSP to both polarities N4 and P5. The top left panel in Figure 5 shows the moment when the PSP footpoints are located entirely in the negative area$R_{SS} = 1.6$, $R_\odot$: the beginning of the transition period T4. 12 hours later (top right panel) the transition is in progress and PSP connects to both polarities when including solar wind speed fluctuations up to $\pm$ 80 km s^{-1}. To establish the best fit and the maximum fit the SS was brought farther all the way up to $R_{SS} = 2.0$ $R_\odot$ (Fig. 5, bottom left panel), and found that the transition was lost. Therefore, the bottom right panel in Figure 5 shows the modeling for $R_{SS} = 1.8$ $R_\odot$ made for the next day November 15,
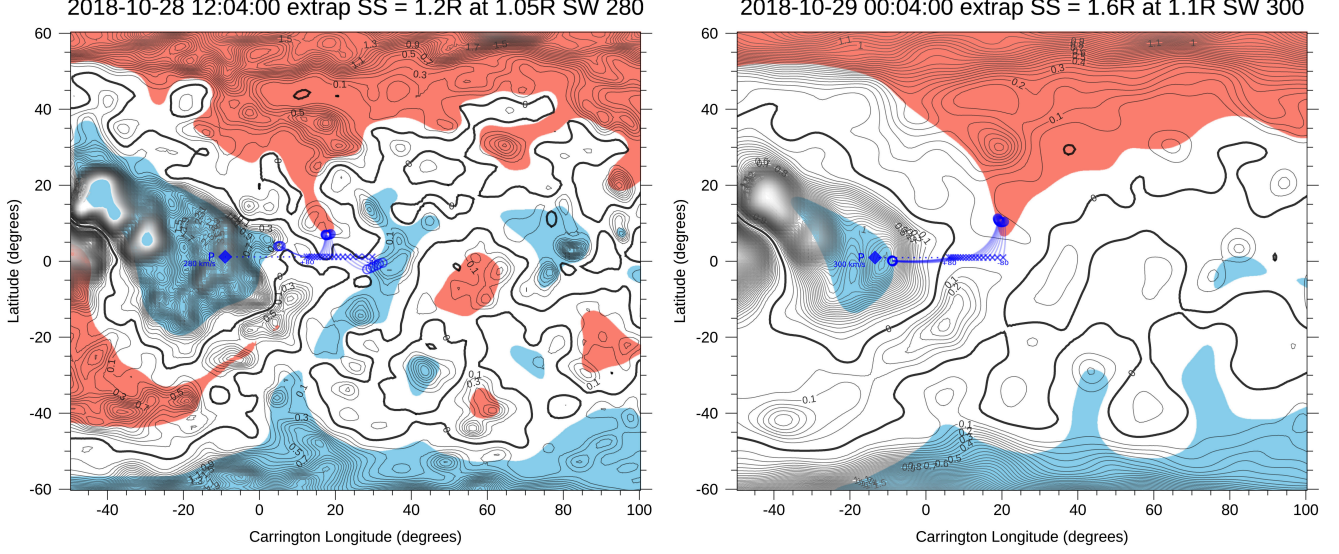
Figure 4. PFSS B^2 contour maps and solar wind foot-points along the PSP trajectory for polarity transition period T3. The projection of PSP location (blue diamond) on the source surface (blue crosses) and down to the solar wind source region (blue circles) calculated for the height R = 1.05.$R_\odot$ and solar wind speed 280 (left) and 300 (right) $\pm$ 80 km s^{-1}. The maps and projections calculated for R_{SS} = 1.2 $R_\odot$ (left, transition N3/P4) and R_{SS} = 1.6 $R_\odot$ (right, transition P4/N4). Open magnetic field regions shown in blue (negative) and red (positive), the neutral line is in bold.

Table 2. Source surface height above T1-T7 (in $R_\odot$)

	T1	T2	T3.1	T3.2	T4	T5	T6	T7
R_{SS}	1.4	1.4	1.2	1.6	1.6	1.4	1.6	2.5
R^*_{SS}	1.6	1.6	1.3	1.8	1.8	1.5	1.8	2.5
$B_{1.1}$, G	1.8-2.2	1.4-2	0.2 - 0.4	1.2-1.4	0.6-1.2	0.2-0.4	4.0	30 (sunspot)

R_{SS} - best fit, R^*_{SS} - max, $B_{1.1}$ is B_r at 1.1 $R_\odot$

2018, the maximum workable source surface height for this region.

Figure 6 illustrates the transition T5 (P5/N5), which was fast (hours) and without polarity fluctuations. This can be explained by the fact that PSP was flying further from the Sun, no longer in quasi-corotation regime as it had been over T3 and T4, which are the beginning and end of the corotation. The simplicity of the transition period T5 allowed straightforward modeling of the footpoint connection to opposite polarities of the relatively weak magnetic field area. The left panel shows the optimal PSP connection with both polarities for R_{SS} = 1.4 $R_\odot$, the right panel shows how this transition nearly disappeared when the source surface height increased up to R_{SS} = 1.6 $R_\odot$.

Figure 7 illustrates the transitions T6 and T7 during Encounter 2. Polarity transition T6 was also fast (hours) again because PSP was flying farther from the Sun and not in corotation. The

left panel in Figure 7 shows the PSP connection with both, positive and negative, polarities calculated for R_{SS} = 1.8 $R_\odot$. The right panel in Figure 7 shows the polarity transition T7 across the very strong active region NOAA AR 12738 on 22 April 2019. The SS height was found to be R_{SS} = 2.5 $R_\odot$. This transition was preceded by multiple CMEs originating from the AR, that created a series of magnetic field inversions observed by PSP and indicated in Figure 1 (bottom panel). How CMEs influence PSP connections is discussed in the following Section 2.1.

Table 2 summarizes results for the best estimates of the solar source surface height R_{SS} above the polarity transition regions along the PSP trajectory during the first encounter. The best fit is defined as the height R_{SS} of the SS when the modeled magnetic polarity transition corresponds to the observed by PSP for the given T, even considering variations in the solar wind velocity.
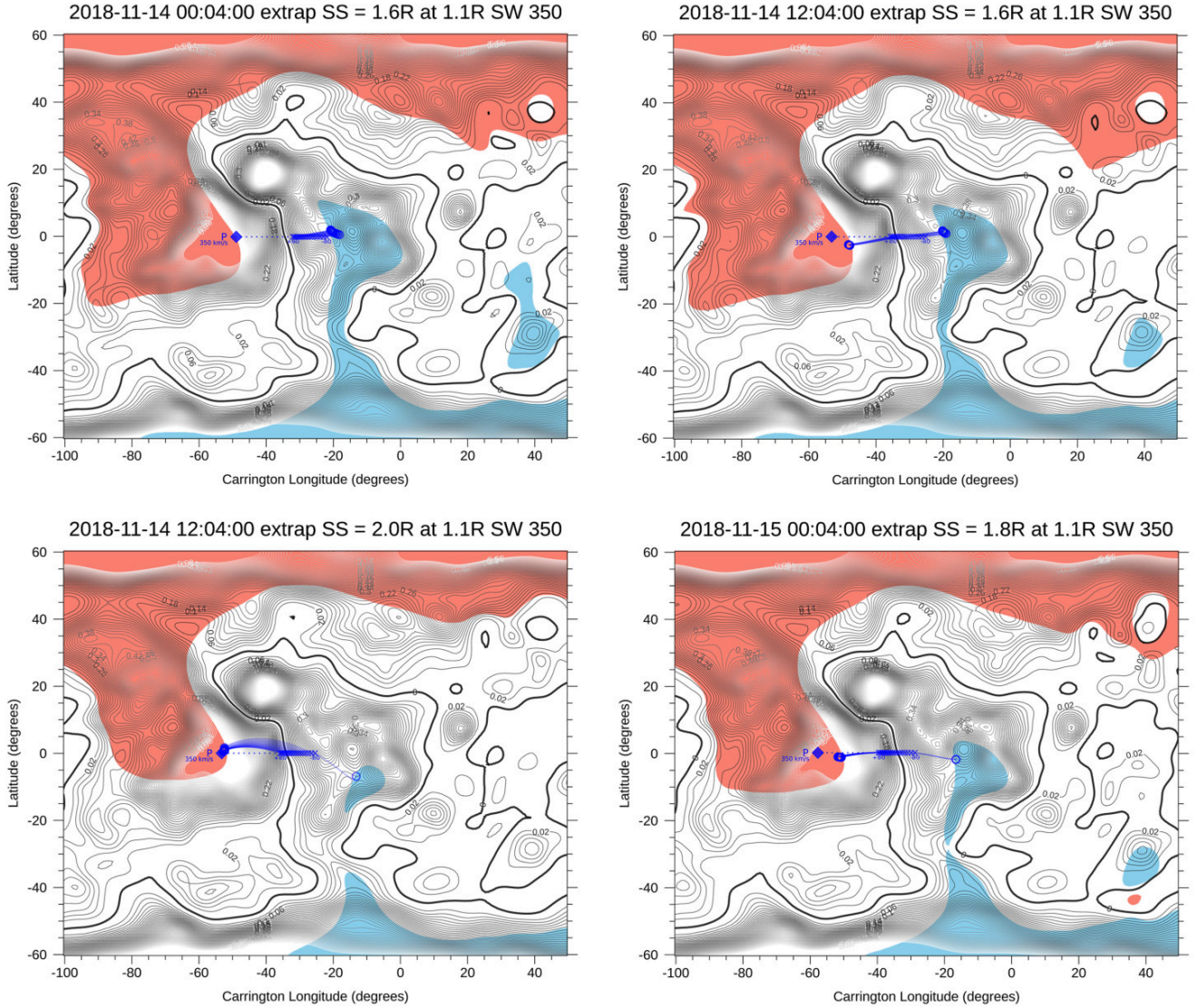
Figure 5. PFSS B^2 contour maps and solar wind foot-points along the PSP trajectory for polarity transition period T4. The projection of PSP location (blue diamond) on the source surface (blue crosses) and down to the solar wind source region (blue circles) calculated for the height R = 1.1.R$_\odot$ and solar wind speed 350 ± 80 km s^{-1}. The maps and projections calculated for three moments of time and three different R$_{SS}$. From left to right, top to bottom panel R$_{SS}$ = 1.6, 1.6, 2.0 and 1.8 $R_\odot$. Open magnetic field regions shown in blue (negative) and red (positive), the neutral line is in bold.

The upper limit value for R_{SS} is the height at which the calculated solar magnetic footpoints of PSP begin to deviate from the observed polarity values. $B_{1.1}$ in Table 2 is the photospheric magnetic field value B_r projected to 1.1 $R_\odot$ by PFSS modeling. $B_{1.1}$ is tabulated for the regions on the Sun where the corresponding polarity transitions (T1 - T7) were taking place.

SS heights right above polarity inversion regions are lower in height, corresponding to dips in the overall non-spherical source surface shape during the current solar minimum. The concept of a non-spherical source surface was introduced by **Schulz et al. (1978)** and developed

further by **Levine et al. (1982)**. Using our results for the best fit R_{SS} above the polarity transition regions T1-T7, a non-spherical SS shape was constructed in correspondence to the PSP solar encounter. The result is show in Figure 8, where the local minimums at the height of R_{SS} above T1-T7 are connected with continuity to the higher source surface positions using quadratic and cubic Bézier curve interpolations. The striking difference in the resulting shapes can be contributed to the different magnetic field magnitude at the photosphere. The source surface, contracted and wrinkled during *E1*, trans-
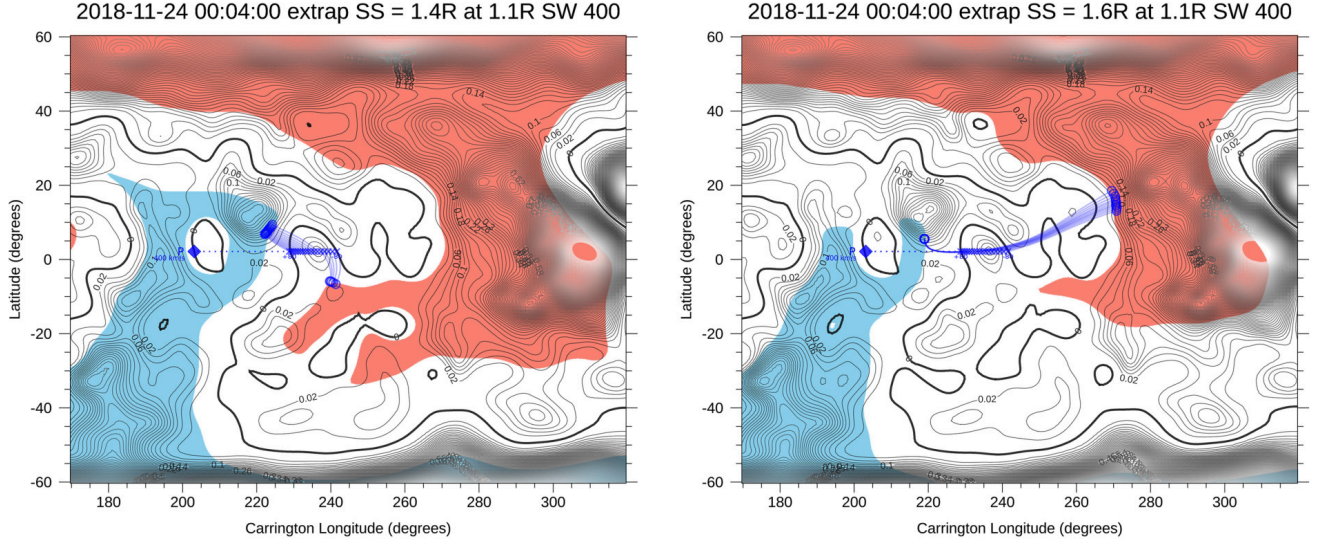
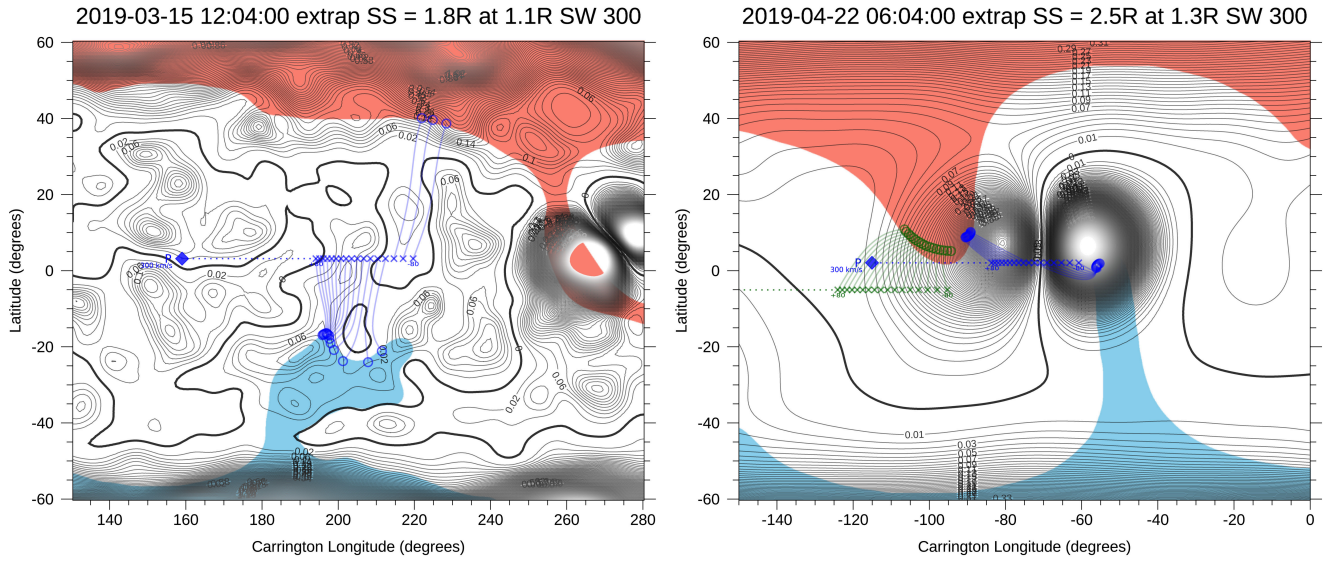**Figure 6.** PFSS B^2 contour maps and solar wind foot-points along PSP trajectory for polarity transition period T5. The projection of PSP location (blue diamond) on the source surface (blue crosses) and down to the solar wind source region (blue circles) calculated for the height R = 1.1 R$_\odot$ and solar wind speed 400 ± 80 km s^{-1}. The maps and projections calculated for the different R$_{SS}$. From left to right panel R$_{SS}$ = 1.4, 1.6$R_\odot$. Open magnetic field regions shown in blue (negative) and red (positive), the neutral line is in bold.

Figure 7. PFSS B^2 contour maps and solar wind foot-points along PSP trajectory for polarity transition periods T6 (left) and T7 (right). The projection of PSP location (blue diamond) on the source surface (blue crosses) and down to the solar wind source region (blue circles) calculated for the height R = 1.1 R$_\odot$ and solar wind speed 300 ± 80 km s^{-1}. The maps and projections calculated for the different R$_{SS}$. From left to right panel R$_{SS}$ = 1.8, 2.5$R_\odot$. Open magnetic field regions shown in blue (negative) and red (positive), the neutral line is in bold. Earth projections to SS and below shown in green color.
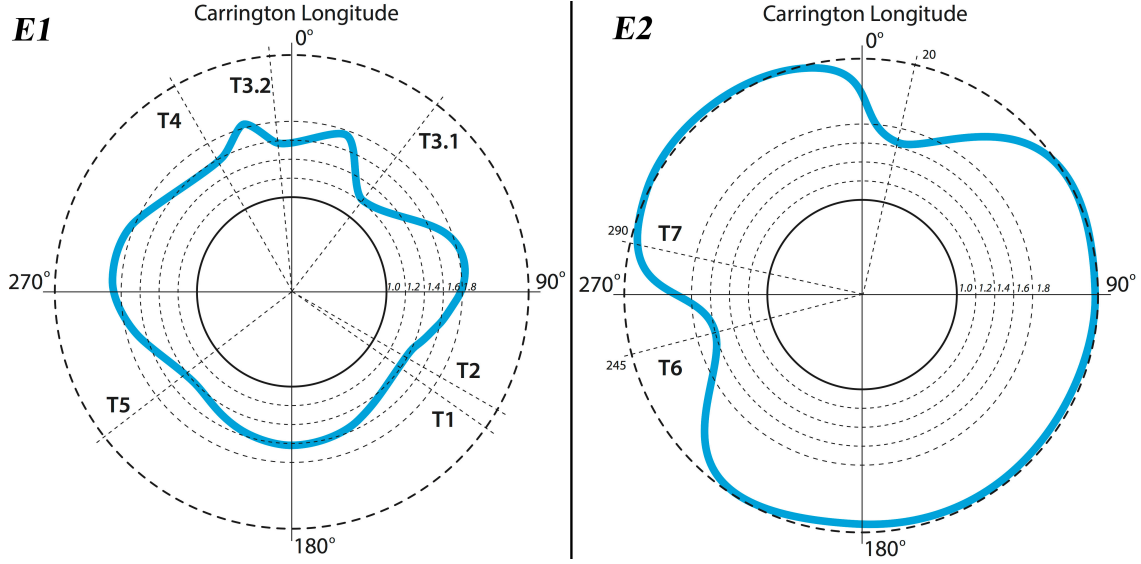
Figure 8. Longitudinal cut for the source surface height calculated from the measured photospheric magnetic field and PFSS modeling along the PSP trajectory during E1 and E2. The solid circle inside each panel is the sun; the outer dash circle has the radius of $2.5R_\odot$. Probe was moving counterclockwise from T1 to T5 during E1, and from T6 to T7 for E2.
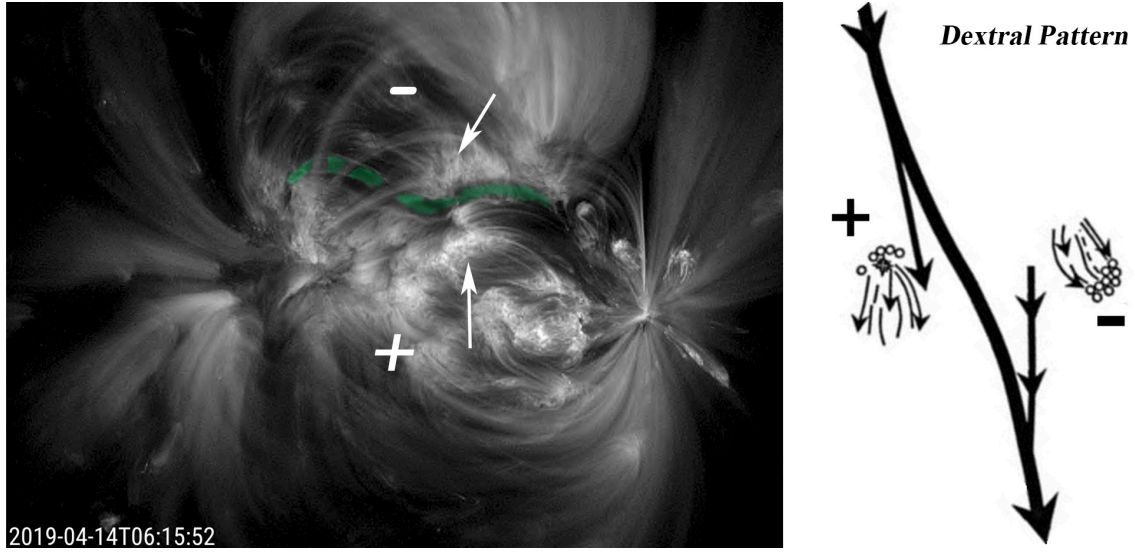

Figure 9. Active region NOAA AR 12738 with a filament (green shade) under the overlying coronal arcade with a skew corresponding to a dextral filament channel. Shown here are coronal cells on both sides of the filament (two representative cells are indicated by the white arrows): note that the cells on opposite sides of the filament channel have cusp-shaped tops that are in opposite directions. They do not cross the channel but follow the same pattern as chromospheric fibrils within a dextral filament channel as depicted in the schematic representation in the right (Sheeley et al. 2013, Panasenco et al. 2013)). Coronal cells form at heights $\sim$ 6 - 10 Mm (Sheeley and Warren, 2012), much lower than average filament heights $\sim$ 50 - 70 Mm. The SDO/AIA 193 Å image is from 14 April 2019 06:15 UT.

formed into the nearly classical **2.5** $R_{\odot}$ **source surface during** *E2*. **Since these changes happened over a very short period of time between two encounters and can not be attributed to different phases of the solar cycle, the explanation must lie in time-dependent changes in the magnetic activity at the sun in** *E2*. **During Encounter 2 in April 2019 the large scale complex active region NOAA AR 12738 with a sunspot developed, together with a smaller but also relatively strong active region NOAA AR 12737. The active regions were separated by** $120°$ **in longitude. Such presence was sufficient to inflate the source surface back to a nearly classic spherical shape with** R$_{\mathrm{SS}}$ = 2.5 R$_{\odot}$ **except for two remaining dips**. In Section 3 we use the best fit R_{SS} height to find the solar sources of the Alfvénic slow solar wind observed at 1 AU during the first PSP encounter and model how these regions were connected to PSP.

2.1. *Influence of CMEs on PSP connectivity*

Panasenco et al. (2013) found that the coronal cells observed and modeled by Sheeley and Warren (2012), do not cross the polarity reversal boundary within a filament channel at the heights below the filament spine top. Coronal cells originate from the network field concentrations and show the same patterns as chromospheric fibrils because they follow the same filament channel magnetic topology, with a strong component of the field parallel to the photosphere. The direction of the axial field inside the filament channel and, therefore, its chirality can be deduced from the geometry of chromospheric fibrils and coronal cells, as shown in Figure 9, illustrating active region NOAA AR 12738 and a filament channel that caused multiple CMEs. One of the CMEs is shown in Figure 10, captured by LASCO/C2. The chirality of CMEs then defines the polarity of the transient coronal hole formed on eruption, and therefore the polarity of the field connecting to PSP during a CME passage. A dextral filament channel means that the direction of the axial magnetic field bears right when viewed from the positive polarity side. It means that the CME's axial magnetic field, when measured in-situ by Probe, was directed from the positive to negative polarity parts of AR 12738. In other words, during the CME passages in April 15-22, 2019 Parker Solar Probe was momentarily connected to transient coronal holes with positive polarity. The num-
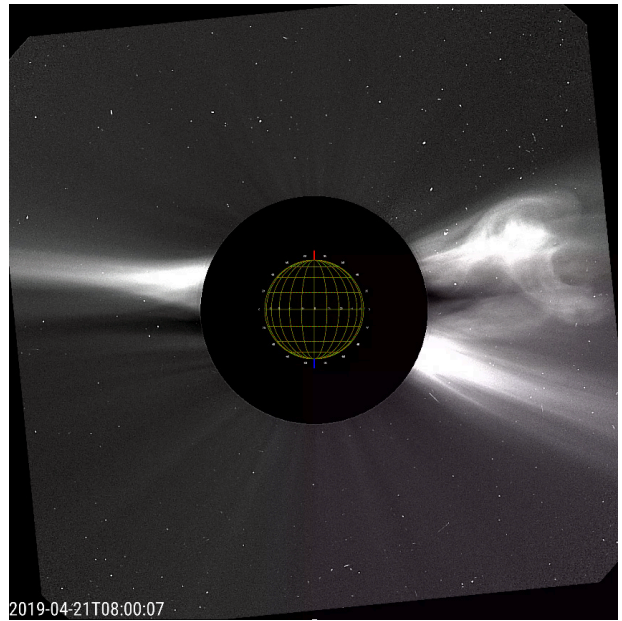

Figure 10. One of the multiple CMEs originating from NOAA AR 12738 and observed by LASCO/C2 on April 21 2019 (a frame from the movie in the online supplementary materials).

ber of positive polarity chunks in Figure 1 (bottom panel) corresponds to the number of CMEs crossing the PSP pass in this time period. PSP reaches the polarity transition period T7 only on April 22, when PFSS modeling connected Probe to the positive polarity of the northern corona hole extension (see Figure 7 for *E2* **connectivity).**

2.2. *Comparison 3D PFSS modeling with the LASCO/C2 coronograph observations*

This section compares the PFSS extrapolations during *E1* **and** *E2* **with LASCO C2 images, to show a direct link between the neutral lines and streamers (as well as pseudostreamer stalks). Superposed on the (occulted) solar disk the PFSS magnetogram is also shown. Figure 11 shows PFSS model results and LASCO/C2 for** *E1*: **the superposition of the neighboring streamer and pseudostreamer (left panel) resulted in merging two of these structures in the coronograph observations. However one two separate pseudostreamer stalks separated as a thin rays may be seen in the coronograph images. Both pseudostramers are leaning into the equatorial streamer. stalk are curved in both the PFSS model and white light LASCO/C2 images, due to a weak magnetic field and lower source surface heights during** *E1* **and the northern coro-**

nal hole super radial expansion. **Figure 12 shows PFSS extrapolation and a LASCO/C2 for period *E2*: the area between the streamer and pseudostreamer stalk is the open coronal field of the small coronal hole of negative polarity originating near the center of the sunspot inside active region NOAA AR 12738. This active region produced multiple CMEs erupting from under the streamer, also it produced multiple transients and flares with plasma propagating into the open field at the pseudostreamer environment. This might explain the apparent asymmetry in the pseudostreamer appearance at the limb, where the northern half is illuminated with more dense plasma and the southern half appears to be completely empty.**

3. ANALYSIS OF THE ALFVÉNIC SLOW WIND SOURCE REGIONS

Throughout the first perihelion encounter, the solar wind as measured by PSP was dominated by large amplitude Alfvénic fluctuations. This is well documented, e.g., in the papers by Horbury et al. (this issue), Matteini et al. (this issue). Quantitatively, if we define the Elsasser variables

$$\vec{z}^{\pm} = \vec{v} \mp \text{sign}(B_r)\vec{b}/\sqrt{(4\pi\rho)},$$

where r denotes the radial component of the large-scale magnetic field B, while v, b denote velocity and magnetic field fluctuations and ρ is the plasma density, purely outwardly propagating Alfvén waves have $\vec{z}^{-} = 0$. In terms of the normalized velocity magnetic field correlation,

$$\rho_{v-b} = \frac{\vec{v} \cdot \vec{b}}{|\vec{v} \cdot \vec{b}|}$$

this means that $\rho_{v-b} = +1$ for outwardly propagating Alfvénic fluctuations along a negative polarity magnetic field line anchored at the Sun, while $\rho_{v-b} = -1$ for outwardly propagating Alfvénic fluctuations along a positive polarity magnetic field line anchored at the Sun. A state with $|\vec{z}^{-}| \ll |\vec{z}^{+}|$ and $|\rho_{v-b}| \geq 0.5$ is called Alfvénic. Additional properties of Alfvénic fluctuations are that the fluctuations of magnetic field magnitude are much smaller than the magnetic field fluctuation amplitudes, and that relative density fluctuations are strongly suppressed with respect to the typical value in a turbulence flow, i.e. the squared turbulent Mach number.

Figure 13 (left panel) shows solar wind measurements at 1 AU over the period encompassing the first PSP perihelion. The left hand side shows an interval of slow wind detected by the Three-Dimensional Plasma and Energetic Particle Investigation (3DP) (Lin et al. 1995) at

~24s resolution and magnetic field measurements sampled by the Wind Magnetic Field Investigation (MFI) (Lepping et al. 1995) interpolated to the time of the plasma measurements, both on board WIND spacecraft, from 20 to 25 October 2018. The upper panel displays the solar wind speed profile, V_{SW} (in km s^{-1}); in the middle panel the v-b correlation coefficient, ρ_{v-b}, is computed at the 1 hr scale typical of Alfvénic fluctuations; the bottom panel shows the magnetic field magnitude, B (in nT). One sees that the velocity magnetic field correlation fluctuates strongly, with very few periods in which it stably strongly either positive or negative. This interval 20 - 25 October, 2018 is characterized by a slow solar wind with a speed ranging between 300 and 400 km s^{-1}, and it is described by a very low v-b correlation coefficient overall. The most Alfvénic part is from day 23 to 23.5 with an average value of -0.87 which corresponds also to a period of almost constant magnetic field magnitude. The right hand side of Figure 13 shows, in the same format and for the same instruments, the time series of the same parameters from 1 to 6 November 2018. In this case, the speed profile shows a transition from a slow wind characterized by a speed around 350 km s^{-1}, a stream interface followed by a faster stream at the end of the interval reaching values around 600 km s^{-1}. In this case, the v-b correlation coefficient moves from values around 0 in the stream interface where we also observe a strong compression of the magnetic field magnitude, to values around -1, in the fast wind.

To connect selected solar wind streams observed at 1 AU to their sources at the Sun we use the same method as in Section 2, when we found magnetic footpoints for the PSP observations of the magnetic polarity inversion periods: we project the spacecraft (i.e. Wind, or the Earth's) position to the source surface via the Archimedean spiral with the given solar wind velocity, and from the source surface down to the selected height above the solar surface along PFSS magnetic field lines. For each stream we use the source surface height as determined in Section 2 for specific areas in the low solar corona.

Figure 14 shows the source region for the Alfvénic slow wind (measured at 1 AU) plotted for two different source surface radii R$_{SS}$ = 1.4, 1.6 $R_{\odot}$ - the best fit and the maximum possible fit for R$_{SS}$ as estimated from Figure 2 for this region. The projection of Earth to the source surface (green crosses) and down to the height R = 1.1.R$_{\odot}$ (green circles) shows that Earth was connected over this time to positive and negative open field areas close to an activity region with relatively strong magnetic field. As shown in Figure 13, the October 23 Alfvénic slow solar wind stream has negative ρ_{v-b}, which
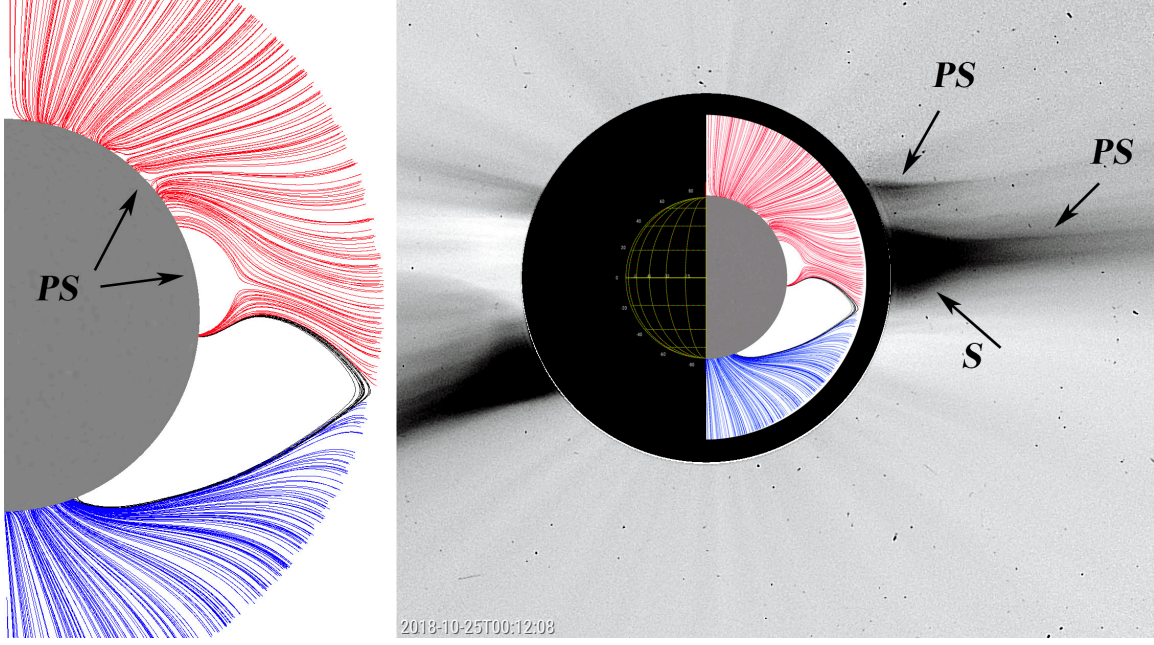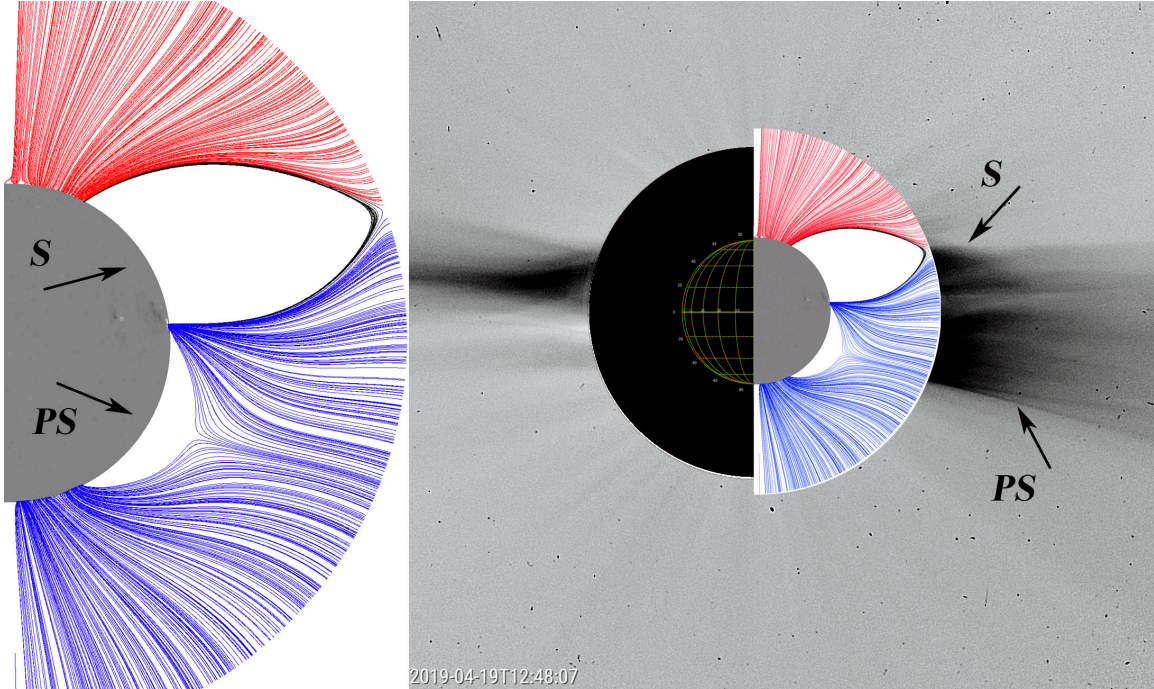
Figure 11. Left panel: Solar magnetogram on disk with open magnetic field lines obtained via PFSS and $R_{SS} = 2.0\ R_\odot$ on 25 October 2018 00:04 UT using SDO/HMI data (during *E1*). The PFSS reconstructed magnetic field configuration is shown as it appears on the limb, and consists of a streamer and two pseudostreamers. Right panel: a composite view of two images, one by the LASCO/C2 camera taken on 25 October 2018 00:12 UT, and one of the PFSS image from the left panel. The modeled streamer and pseudostreamer positions correspond well to the ones observed by LASCO/C2.

Figure 12. Left panel: solar magnetogram on disk with open magnetic field lines obtained via PFSS and $R_{SS} = 2.5\ R_\odot$ on 9 April 2019 12:04 UT using SDO/HMI data (during *E2*). The PFSS reconstructed magnetic field configuration is shown as it appears on the limb, and consists of a streamer and a pseudostreamer. Right panel: a composite view of two images, one by the LASCO/C2 camera taken on 19 April 2019 12:48 UT, and one the PFSS image from the left panel. The modeled streamer and pseudostreamer positions correspond well to the ones observed by LASCO/C2.
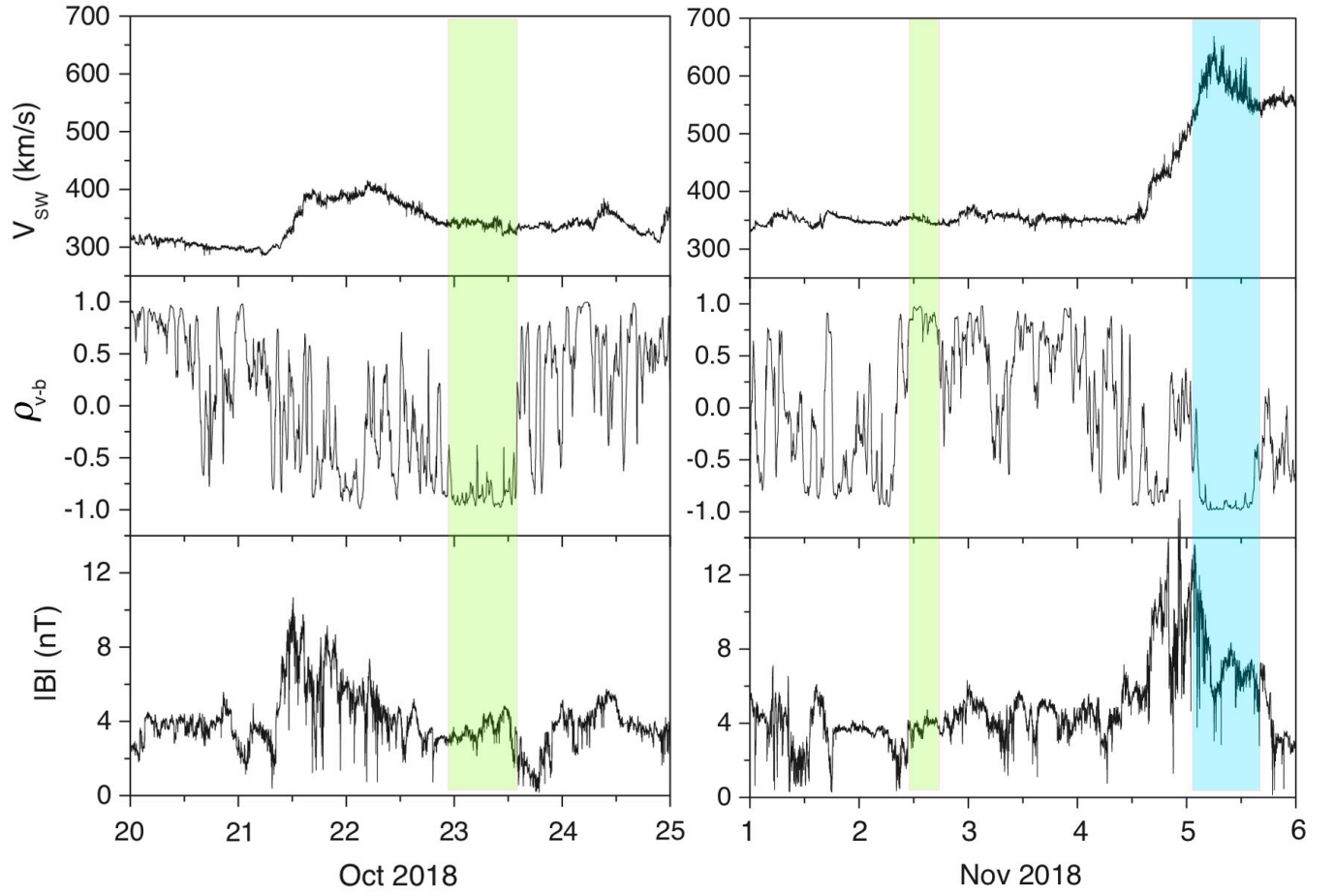
Figure 13. 1 AU observations. Green shades indicate periods of Alfvénic slow solar wind in Oct 23 and Nov 2, blue area indicate Alfvénic fast wind in Nov 5. (left) from top to bottom, Wind/3DP time series of solar wind speed, V_{SW} (in km/s); v-b correlation coefficient, ρ_{v-b}, computed at 1 hr scale; magnetic field magnitude, B (in nT) from the Wind/MFI instrument for the interval 20 - 25 October, 2018. (right) the same parameters for the interval 1 - 6 November, 2018. The Alfvénic slow wind is highlighted in green while the fast wind in blue.
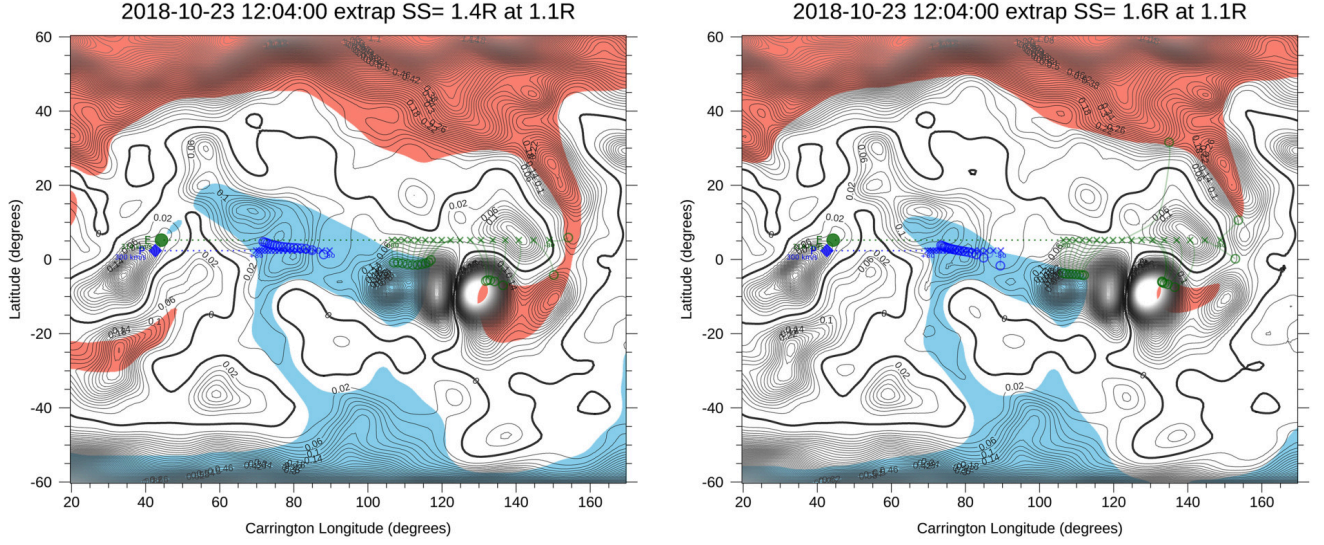
Figure 14. PFSS B^2 contour maps and solar wind foot-points for Earth and PSP trajectory for origins of Alfvénic slow solar wind at 1 AU selected in Fig. 7, Oct 23, 2018 . The projection of Earth (green circle) and PSP (blue diamond) on the source surface (blue crosses) and down to the solar wind source region (blue circles) calculated for the height R = 1.1.R$_\odot$. The maps and projections calculated for the different R$_{SS}$. From left to right panel R$_{SS}$ = 1.4, 1.6 $R_\odot$ and correspond to the best fit source surface calculated in Section 2. Open magnetic field regions shown in blue (negative) and red (positive), the neutral line is in bold.
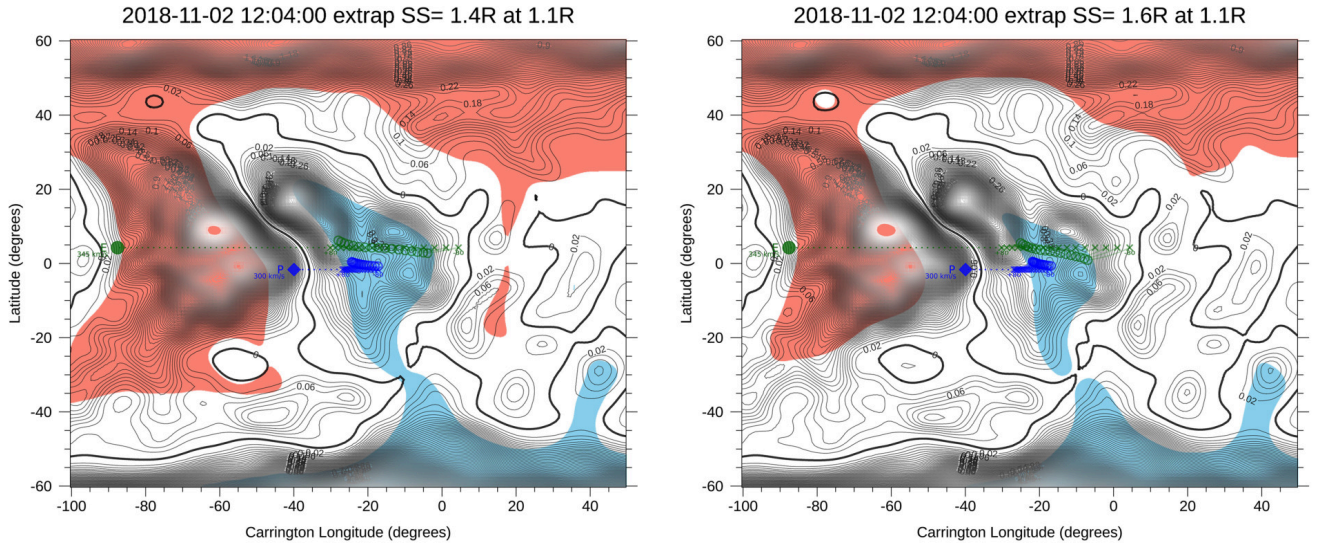

Figure 15. PFSS B^2 contour maps and solar wind foot-points for Earth and PSP trajectory for origins of Alfvénic slow solar wind at 1 AU selected in Figure 7, Nov 2, 2018 . The projection of Earth (green circle) and PSP (blue diamond) on the source surface (blue crosses) and down to the solar wind source region (blue circles) calculated for the height R = 1.1.R$_\odot$. The maps and projections calculated for the different R$_{SS}$. From left to right panel R$_{SS}$ = 1.4, 1.6 $R_\odot$ and correspond to the best fit source surface calculated in Section 2. Open magnetic field regions shown in blue (negative) and red (positive), the neutral line is in bold.
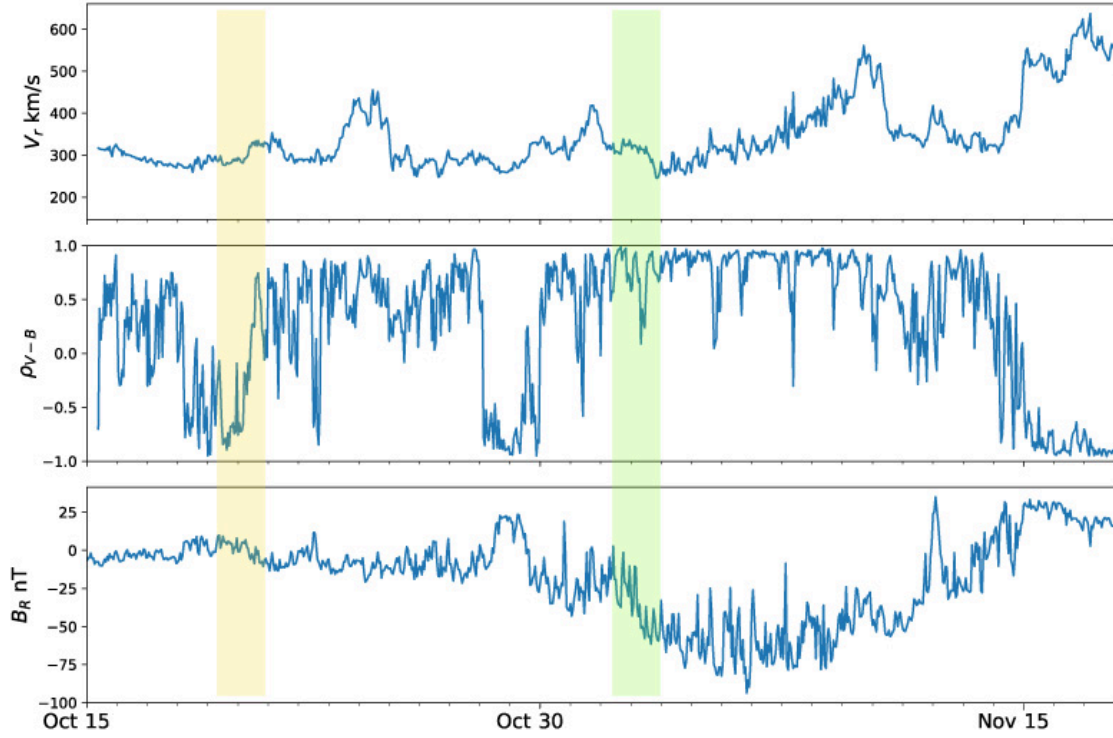
Figure 16. PSP observations during the interval 15 Oct - 18 Nov, 2018. Yellow shade indicates periods Alfvénic slow solar wind on 20 October originated from the same region and propagated from PSP to 1AU, arriving at 1 AU on 23 October (Fig. 13, left panel and Fig. 14). Green shade indicates periods of Alfvénic slow solar wind on 2 November originated from the same region and measured at the same time at PSP and 1AU (Fig. 13, right panel and Fig. 15). From top to bottom, PSP solar wind speed, V_r (in km/s); v-b correlation coefficient, ρ_{v-b}, computed at 1 hr scale; magnetic field magnitude, B (in nT).

corresponds to a positive magnetic field. Therefore, the area from where this Alfvénic slow solar wind stream originated for this day was on the positive polarity side connecting to Earth. PSP observed solar wind from this area during transition period T1 in October 20 as was discussed previously in Section 2.

Figure 15 shows the same measurements but for the second Alfvénic slow wind stream observed on November 2, 2018. This Alfvénic slow solar wind stream has positive ρ_{v-b} and therefore originated from a negative magnetic polarity region on the Sun. The Probe magnetic footpoints were in the same area for nearly two weeks as well as on November 2, 2018, when Earth also remained connected to this area.

Figure 16 shows the PSP measurements during the interval 15 Oct - 18 Nov, 2018, the three panels from top to bottom showing wind speed, the ρ_{v-b}, and radial magnetic field respectively. Yellow shading indicates periods of Alfvénic slow solar wind on October 20th that originated from the same region on the Sun (Figures 2 and 14) and propagated from PSP to 1AU, arriving at 1 AU on October 23rd (Fig. 13, left panel) where it was seen at Earth. The wind appears to undergo only a slight acceleration, from 320 to 350 km/s over the PSP - 1 AU distance. Green shading shows an Alfvénic slow wind stream at PSP and 1 AU for November 2, 2018: this is wind from the same solar source (Fig. 15), observed at the same time, but different plasma parcels. A similar very slight acceleration is observed.

The Alfvénic fast solar wind stream shown in blue color shade on November 5, 2018 in Figure 13 has a negative correlation ρ_{v-b} and the corresponding Earth magnetic footpoints were anchored inside a positive open field area as shown in Figure 17. The Earth's position extrapolates backwards into the middle of the equatorial extension of the positive Northern polar corona hole. The source surface where the magnetic field becomes radial was selected in accordance with the "best fit" results described in Section 2 and was selected to be R_{SS} = 1.6 $R_\odot$. 3D PFSS models in Figures 18-20 correspond to the 2D magnetic pressure maps shown in Figures 14, 15, 17.

The first slow Alfvénic stream, observed on 23 October, 2018 at 1 AU, originated from a pseudostreamer configuration, more precisely from its southern coronal hole indicated by the black arrow in Figure 18. This is the same positive open field region shown in Figure 14 and to which Earth was magnetically connected (green circles). The very non-monotonic expansion of the open magnetic field appears to have a funnel-like
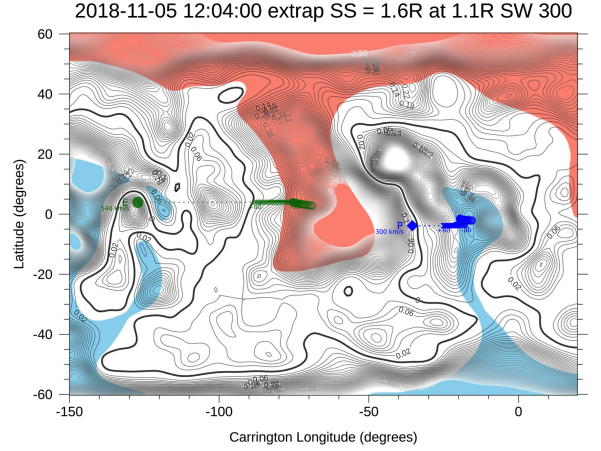

2018-11-05 12:04:00 extrap SS = 1.6R at 1.1R SW 300

Figure 17. PFSS B^2 contour map and solar wind footpoints for Earth and PSP trajectory for origins of Alfvénic fast solar wind stream at 1 AU selected in Figure 13 (right panel; Nov 5, 2018). The projection of Earth (green circle) and PSP (blue diamond) on the source surface (blue and green crosses) and down to the solar wind source region (blue and green circles) calculated for the height R = 1.1.$R_\odot$. The map and projections calculated for R_{SS} = 1.6 $R_\odot$ and correspond to the best fit source surface calculated for this region in Section 2. Open magnetic field regions shown in blue (negative) and red (positive), the neutral line is in black bold.

topology, similar to the geometry of the field described in Panasenco et al. (2019), that might explain its very low speed.

The second slow Alfvénic wind stream originated from an equatorial coronal hole with relatively strong magnetic field. The very complicated topology near the base of this open field area includes multiple small-scale pseudostreamers whose branches converge and diverge in the direction perpendicular to the equator (Fig. 19). On the other hand, the coronal hole from where the Alfvénic fast wind originated presented by a very smooth and monotonically expanding magnetic field (Fig. 20). These results suggest that for the origin of slow Alfvénic streams highly expanding open coronal fields are a requirement.

4. CONCLUSIONS

The Parker Solar Probe trajectory over its first perihelion pass brought it to traverse different regions on the Sun with different solar wind sources. A range of the solar source surface heights R_{SS} = 1.2 - 1.8 $R_\odot$ was required to correctly reproduce polarity transition periods during *E1*, and 1.6 - 2.5 for *E2*, showing that source-surface extrapolations generally require a non-spherical outer boundary, as illustrated in Figure 8. The source surface heights above the polarity inversion regions are
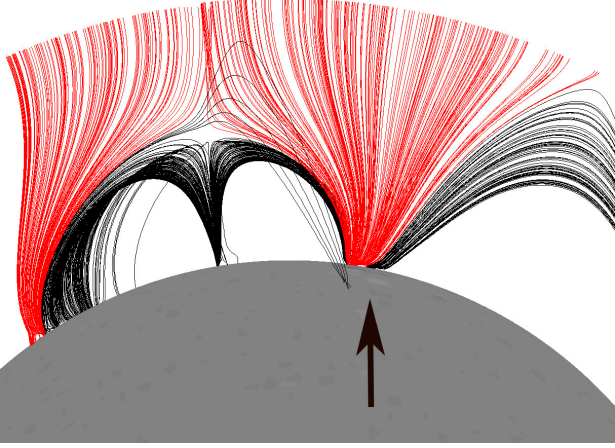
Figure 18. 3D PFSS model for the area of the origin of Alfvénic slow solar wind observed at 1AU on Oct 23, 2018 (corresponds to the map in Figure 14).
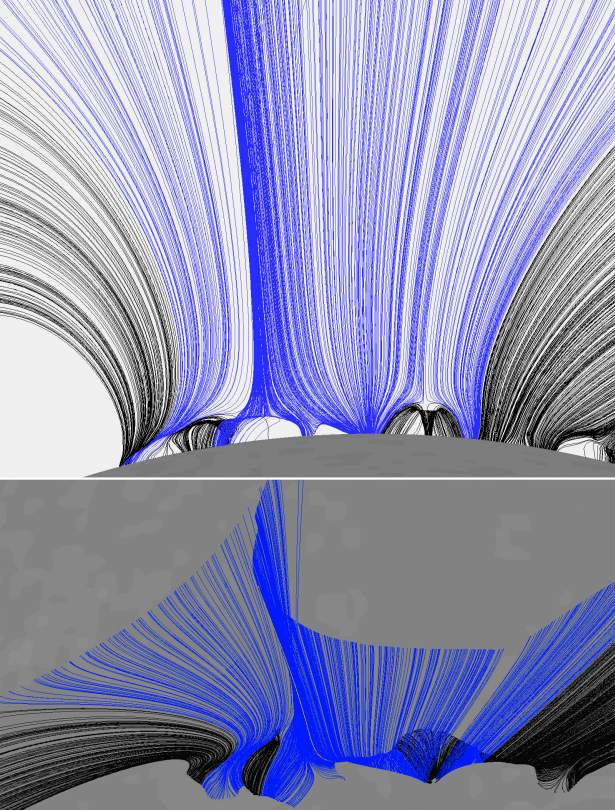

Figure 19. 3D PFSS model for the area of the origin of Alfvénic slow solar wind observed at 1AU on Nov 02, 2018 (corresponds to the map in Figure 15).

the local dips or minimums in the overall non-spherical source surface shape during the current solar minimum.

Although the perihelion passage occurred during a time of deep solar minimum, and the magnetic field on the Sun was globally very weak, different types of solar wind were observed. Around perihelion and inside coro-
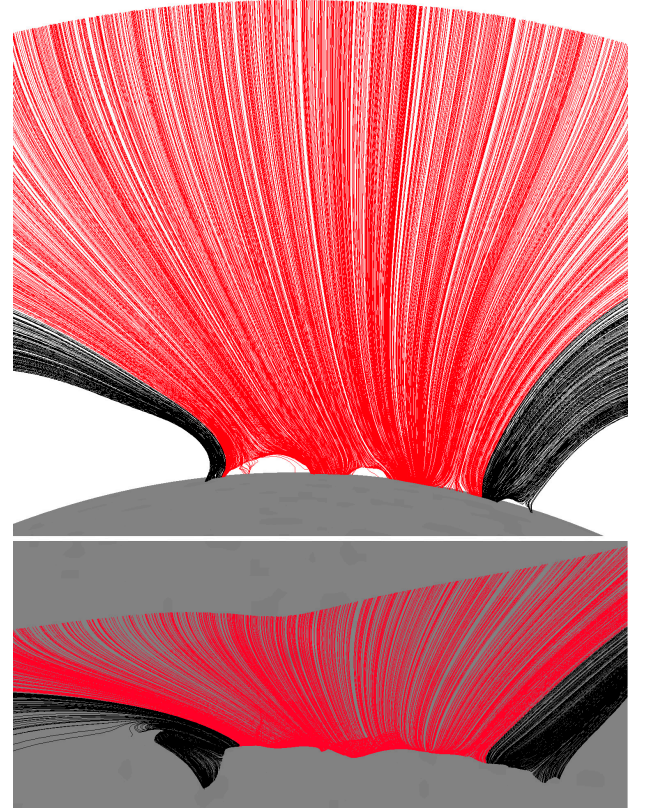

Figure 20. 3D PFSS model for the area of the origin of Alfvénic fast solar wind observed at 1AU on Nov 05, 2018 (corresponds to the map in Figure 17)

tation, PSP traversed a very small negative coronal hole (or coronal hole extension) prograde and retrograde, observing slow wind dominated by outwardly propagating Alfvénic turbulence throughout the encounter. It also saw faster Alfvénic wind streams before and after. The detailed properties of the waves, large scale wave-packets including the so-called switchbacks and radial jets are detailed elsewhere (Horbury et. al., this issue, Matteini et al. this issue). Such fluctuations in the presence of extremely slow wind are not a common occurrence at greater heliocentric distances, where Alfvénic slow wind is seen more commonly at solar maximum appearing to originate from so-called magnetic funnels (Panasenco et al., 2019). Here we see that the open region crossed at perihelion also has very large expansion factors, while more standard radially expanding regions remain Alfvénic with faster winds.

Using the best fit for R_{SS} we also traced back to the Sun the short Alfvénic slow wind streams observed at 1 AU, found their source regions and created the 3D PFSS models for the coronal field in these regions. These models reveled the peculiar topology in both cases - coronal pseudostreamers large and smaller scales. We found that only small regions of wind remained Alfvénic out to

1AU, one of which corresponded to the fast expanding open region at the PSP perihelion.

Our findings confirm an important property of the coronal magnetic field, namely that small regions in the corona, in the presence of complex fields structure at the Sun (i.e. largely non dipolar fields) can expand super-radially to occupy large regions of the Heliosphere. Our finding also show that Alfvén waves may be an important part of most of the nascent solar wind, with the Alfvénicity decreasing rapidly with distance from the in streams close to the equator and the heliopheric current sheet, and surviving out to greater distances only in the fast wind from dominant polar coronal holes or in the slow wind from rapidly super-radially expanding small open "funnel" regions. Further research will show whether these regions, often presenting multipolar pseudostreamer configurations at their base, may be identified by other tracers, including compositional differences, in the solar wind. To this end, joint observations with the upcoming Solar Orbiter together with Parker Solar Probe will help to shed light on the generation and acceleration of different solar wind stream types.

REFERENCES

Abbo L., Ofman L., Antiochos S. K., et al., 2016, SSRv, 201, 55, doi:10.1007/s11214-016-0264-1

Antonucci E., Abbo L. & Dodero M. A., 2005, A&A, 435, 699

Badman et al. 2020 (this issue)

Bale, S. D., Goetz, K., Harvey, P. R., et al. 2016, SSRv, 204, 49

Bale, S. D., Badman, S.T., Bonnell, J.W. et al. 2019, Nature (doi:10.1038/s41586-019-1818-7)

Belcher J. W. & Davis L., 1971, J. Geophys. Res., 76, 3534

Belcher J. W. & Solodyna C. V., 1975, J. Geophys. Res., 80, 181

Bruno R., & Carbone V., 2013, LRSP, 10, 2

D'Amicis R. & Bruno R., 2015, ApJ, 805, 84:1

D'Amicis, R., Matteini, L., Bruno, R. 2019, MNRAS, 483, 4665

Fox, N. J., Velli, M. C., Bale, S. D., et al. 2016, SSRv, 204, 7

Geiss, J., Gloeckler, G., & von Steiger, R. 1995, SSRv, 72, 49

Horbury et al. 2020 (this issue)

Janardhan, P., Fujiki, K., Ingale, M., et al. 2018, A&A, 618, A148

Ko, Y.-K., Roberts, D. A., & Lepri, S.T. 2018, ApJ, 864, 139

Lee, C. O., Luhmann, J. G., Hoeksema, J. T., et al. 2011, SoPh, 269, 367

Lepping, R. P., Acuña, M. H., Burlaga, L. F., et al. 1995, Space Sci. Rev. 71, 207

Levine, R. H., Altschuler, M. D., Harvey, J. W., et al. 1977, ApJ, 215, 636

Levine, R. H., Schulz, M., & Frazier, E. N. 1982, SoPh, 77, 363

Lin, R. P., Anderson, K. A., Ashford, S., et al. 1995, Space Sci. Rev., 71, 125

Marsch, E., Rosenbauer, H., Schwenn, R., et al. 1981, JGR, 86, 9199

Matteini, L., Horbury, T.S., Pantellini, F., Velli, M. and Schwarz, S.J., 2015, ApJ 802:11

Matteini et al. 2020 (this issue)

Neugebauer M., Goldstein B. E., Smith E. J., Feldman W. C., 1996, JGRA, 101, 17047

Panasenco, O., & Velli, M. 2013, in AIP Conf. Proc. 1539, Solar Wind 13, ed. G. P. Zank et al. (Melville, NY: AIP), 50

Panasenco, O., Martin, S. F., Velli, M., et al. 2013, SoPh, 287, 391

Panasenco, O., Velli, M., & Panasenco, A. 2019, ApJ, 873, 25

Platten, S. J., Parnell, C. E., Haynes, A. L., et al. 2014, A&A, 565, A44

Perrone, D., D'Amicis, R., De Marco, R., et al, submitted to A&A

Scherrer, P. H., Schou, J., Bush, R. I., et al. 2012, SoPh, 275, 207

Schou, J., Scherrer, P. H., Bush, R. I., et al. 2012, SoPh, 275, 229

Schrijver, C. J., & De Rosa, M. L. 2003, SoPh, 212, 165

Schulz, M., Frazier, E. N., & Boucher, D. J. 1978, SoPh, 60, 83

Schwenn, R. 1990, Physics of the Inner heliosphere I – Large scale structure of the interplanetary medium, editors: R. Schwenn and E. Marsch, Springer-Verlag Berlin Heidelberg

Sheeley, N. R., & Warren, H. P. 2012, ApJ, 749, 40

Sheeley, N. R., Martin, S. F., Panasenco, O., et al. 2013, ApJ, 772, 88

Stansby, D., Horbury, T.S., Matteini, L. 2019, MNRAS, 482, 1706

Stansby, D., Matteini, L., Horbury, T. S., submitted to MNRAS

Tu, C.-Y., & Marsch, E. 1995, SSRv, 73, 1

von Steiger, R. 2008, in The Heliosphere Through the Solar Activity Cycle, edited by A. Balogh, L. J. Lanzerotti, and S. T. Suess, chap. 3, pp. 41–78, doi:10.1007/978-3-540-74302-63, Springer Praxis, Chichester, U. K.

Wang, Y.-M. 1994, ApJL, 437, L67

Wang, Y.-M., & Sheeley, N. R. 1990, ApJ, 365, 372

Wang, Y.-M., Sheeley, N. R., Jr., & Rich, N. B. 2007, ApJ, 658, 1340

Wang, Y.-M., & Ko, Y.-K. 2019, ApJ, 880, 146

Wang, Y.-M., & Panasenco, O. 2019, ApJ, 872, 139

Zhao, L., Zurbuchen, T. H., Fisk, L. A., 2009, Geophys. Rev. Lett., 36, L14104